Analysis of the flow structure inside the valveless standing wave pump

Majid Nabavi,[a] Kamran Siddiqui, and Javad Dargahi
Department of Mechanical and Industrial Engineering, Concordia University,
1455 de Maisonneuve Blvd. West, Montreal, Quebec H3G 1M8, Canada

The flow structure inside the valveless standing wave pump is investigated experimentally. The two-dimensional velocity fields inside the chamber of this novel pump at different phases of the excitation signal are measured using the synchronized particle image velocimetry technique. The variations in the pump flow rate, pressure loss coefficients, and rectification capability of the diffuser-nozzle element are analyzed. According to the results obtained in this paper, the net flow rate of the pump increases with an increase in the pressure (or Reynolds number). The interactions of three different flow fields inside the pump chamber (pumping flow, acoustic, and streaming velocities) are studied. It is found that, while the pumping flow has an effect on the acoustic velocity patterns only around the inlet and outlet orifices, the streaming velocity structures are drastically affected by the pumping flow. © *2008 American Institute of Physics*. [DOI: 10.1063/1.3026074]

I. INTRODUCTION

Valveless pumping is an emerging field of research due to the wide range of its applications in different areas of engineering.[1,2] Two kinds of valveless pumps have been extensively investigated experimentally and numerically, which are valveless impedance pump and reciprocating valveless pump. The impedance pump uses a mismatch in impedance to drive fluid. It is comprised of an elastic tube, connected at the ends to a more rigid tubing. By compressing the elastic section periodically at an asymmetric position from the ends, traveling waves are emitted due to compression that can reflect at the impedance mismatch, generating a net flow.[3–5] Recently, Bringley *et al.*[6] constructed a prototype of the valveless impedance pump consisting of a section of an elastic tube and a section of a rigid tube connected in a closed loop and filled with water. They studied the flow rates for various squeezing locations, frequencies, and elastic tube rigidities. They also formulated a simple model that can be described by ordinary differential equations.

The reciprocating valveless pumps consist of two diffuser-nozzle elements on each side of a chamber volume with an oscillating diaphragm. The vibrating diaphragm produces an oscillating chamber volume which, together with the two fluid-flow-rectifying diffuser/nozzle elements, creates a net fluid flow.[7,8]

In this study, a new valveless pumping mechanism called *valveless standing wave pump* (SWP) is developed which achieves a pumping action using the properties of acoustic standing wave. The time-variant two-dimensional velocity fields inside the chamber of this novel pump are analyzed. Furthermore, the interesting phenomena due to the interaction of different velocity fields inside the valveless SWP are analyzed and discussed.

II. DEVELOPMENT OF THE VALVELESS SWP

The valveless SWP can be considered as a new valveless pumping mechanism. It is a device that pumps both gaseous and liquid fluids efficiently without any mechanical moving part and check valve. The device is simple and inexpensive to construct and operate. The valveless SWP is suitable for a wide range of industrial and biomedical applications due to small power consumption, no moving parts, no frictional losses, no lubrication requirement, complete isolation of the fluid from the outside environment, and no chance of fluid contamination. Furthermore, in the valveless SWP there is no chance of mechanical failure and, hence, it is reliable. All of the previously proposed SWPs (Refs. 9–12) need one or more check valves for their operation and, therefore, moving mechanical components are involved. The significant problems associated with these pumps include fatigue of moving valves, clog, high pressure loss of valves, and low driving frequency. Furthermore, no academic research has been conducted on these devices. Of particular interest is the SWP patented to Bishop,[11] which claims to provide pumping action due to properties of acoustic standing wave. The pumping action of this pump requires a check valve at each inlet or outlet. It is also claimed in the above patent that the apparatus is able to pump fluids without a check valve if operated at a nonlinear standing wave region; however, the invention does not provide any supporting evidence for this claim.

Once the standing wave is established in the pump chamber, at the pressure antinode the pressure is oscillating above and below the undisturbed pressure (P_0) of the fluid. For linear standing wave, the pressure oscillations above and below P_0 are approximately equal and the average pressure at the pressure antinode would be equal to P_0. However, in the nonlinear region, the pressure oscillations above and below P_0 become unequal. Consequently, an average pressure greater than P_0 can be obtained at the pressure antinode. The small difference between the average pressure at the pressure

[a]Author to whom correspondence should be addressed. Electronic mail: m_nabav@encs.concordia.ca. Telephone: 514-848-2424. Fax: 514-848-3175.
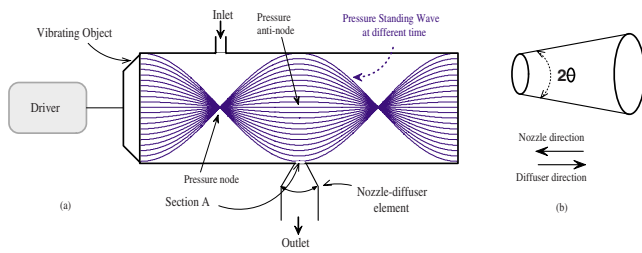
FIG. 1. (Color online) (a) Schematic illustration of the valveless SWP. (b) The conical diffuser-nozzle element.

node and antinode can pump the fluid without using the check valve. However, because of two main reasons, this configuration of a valveless pump is not practical and efficient. First of all, to obtain even a small pressure difference between the average pressure at the pressure node and antinode (consequently very small net flow rate), the pressure amplitude at the antinode should rise to very large values, which is not efficient and practical. Second, at such high pressure fluctuations, several undesirable phenomena such as large amplitude streaming, wave attenuation, and wall vibration occur, which degrade the pumping action and hence reduce the efficiency.

The valveless SWP developed in this study is able to pump fluid efficiently in the presence of a linear or nonlinear standing wave. In addition, unequal pressure oscillations above and below P_0 in the nonlinear case have a positive impact on the pumping action of the valveless SWP. Like other reciprocating valveless pumps,[7] in the valveless SWP the difference between the flow resistance across the diffuser and the nozzle is used to direct the flow to a desired direction. In the previously reported valveless pumps, a moving diaphragm performs pressure work on the working fluid in a periodic manner. However, in the valveless SWP, pressure variation is achieved by establishment of the standing wave inside the pump chamber.

A. Operating principle of the valveless SWP

The valveless SWP consists of a chamber, a vibrating object, a driver, and a diffuser-nozzle element, as illustrated in Fig. 1(a). The operation principle of the valveless SWP is similar to the SWP with a valve.[9–12] The main difference is that in the valveless SWP, instead of a check valve, a diffuser-nozzle element is placed at the outlet. A diffuser is characterized by a gradual widening of the fluidic cross section in the sense of the flow and a smaller fluidic resistance. A nozzle is characterized by a gradual reduction in the fluidic cross section in the sense of the flow and a higher fluidic resistance.

In the linear range of the acoustic wave, the pressure at a pressure antinode, $p(t)$, can be expressed by $p(t) = P_0 + p' \sin(\omega t)$, where p' is the fluctuation amplitude of the pressure [see Fig. 2(a)]. This time-varying pressure is applied at the diffuser-nozzle input (the narrowest part of the diffuser-nozzle element). When $p(t) > P_0$, the pump will be in the discharge mode and the fluid will exit the pump chamber through the diffuser-nozzle element which acts as diffuser in this mode [see Fig. 2(b)]. At the same time, since the inlet is located at the pressure node, the pressure fluctuation at the inlet is almost zero, which means that the pressure at the inlet is almost equal to P_0. Due to the higher fluid pressure outside the chamber at the inlet location, fluid enters the chamber through the inlet. For $p(t) < P_0$, the pump will be in the suction mode and the fluid will enter the pump chamber through the diffuser-nozzle element which acts as nozzle in this mode [see Fig. 2(c)]. With the equal amplitude of pressure fluctuation in the discharge and suction modes due to lower pressure loss (or lower flow resistance) in the diffuser direction than that in the nozzle direction, the volume of the outgoing flow through the outlet element in the discharge mode is larger than the incoming flow in the suction mode. Therefore, there will be a net flow discharge from the diffuser-nozzle element. Thus, fluid pumping is achieved by the valveless SWP. The pumping action of this pump is related to the maximum pressure fluctuation inside the pump
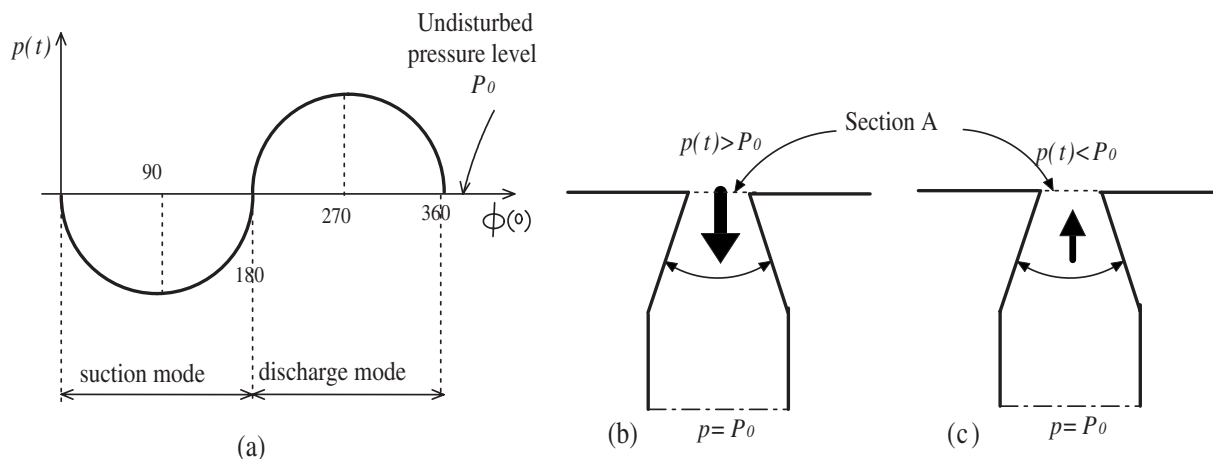

FIG. 2. (a) Pressure fluctuation at the pressure antinode in the linear region. Flow rectification of the valveless SWP in (b) discharge mode and (c) suction mode.

chamber. The larger the pressure fluctuation, the higher will be the net flow rate of the pump. To achieve higher pressure fluctuation, larger vibrational displacement of the acoustic driver is required.

The pumping action of the present valveless SWP enhances in the nonlinear range of the standing wave. In the nonlinear region, the pressure oscillations above and below P_0 are asymmetric. The fluctuation amplitude of the pressure above P_0 is greater than that below P_0. Consequently, the relative difference between the outgoing and incoming flows through the diffuser-nozzle element for the nonlinear case is larger than that for the linear case.

B. Diffuser-nozzle element

In order to achieve the best pump performance, the diffuser-nozzle element has to be designed for the highest possible flow directing capability. The rectification capability (η) of the diffuser-nozzle element can be defined as

$$\eta = \frac{\xi_n}{\xi_d}, \tag{1}$$

where ξ_n and ξ_d are measures of direction-dependent flow resistance and called pressure loss coefficients of the nozzle and diffuser, respectively. These parameters are defined as[7]

$$\xi_n = \frac{2\Delta p}{\rho u_n^2}, \quad \xi_d = \frac{2\Delta p}{\rho u_d^2}, \tag{2}$$

where Δp is the average pressure difference across the diffuser-nozzle element and u_n and u_d are the average flow velocities through the diffuser-nozzle element in the nozzle and diffuser directions, respectively. In order to optimize the efficiency of the diffuser-nozzle element, η should be maximized.

It is noteworthy that, although, in general, the diffuser-nozzle element has a higher pressure loss in the nozzle direction than in the diffuser direction, there are some exceptions to this general rule. For instance, for a large opening angle, the losses are, in fact, higher in the diffuser direction than in the nozzle direction because of a sudden expansion and, thus, the flow directing principle is not based on diffuser pressure recovery.[13] Recently reported experimental results in the steady flow regime show that for Reynolds number of Re=2000 and θ=60°, the rectification capability is less than unity (η=0.97).[14]

III. DIFFERENT VELOCITY FIELDS ASSOCIATED WITH THE VALVELESS SWP

There are three different velocity fields inside the pump chamber of the valveless SWP.

(1) *Acoustic standing wave velocity* or, briefly, *acoustic velocity field*: In the linear range of acoustic intensity studied in this work, the amplitudes of the axial (u) and transverse (v) components of the acoustic velocity are given as
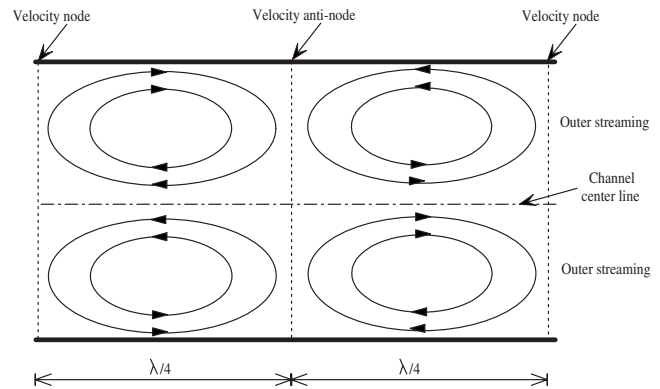

FIG. 3. Schematic of streaming patterns in a channel.

$$u = u_{max} \sin(2\pi x/\lambda), \quad v = 0, \tag{3}$$

where x is the axial coordinate, $u_{max} = P_0/\rho_0 c_0$ is the maximum acoustic velocity, λ is the wavelength, ρ_0 is the density of the fluid, and c_0 is the speed of sound. The fluctuation of the acoustic velocity is maximum at the velocity antinode (or pressure node) where the inlet is located [see Fig. 1(a)]. This fluctuation is almost zero at the velocity node (or pressure antinode) where the outlet is located [see Fig. 1(a)].

(2) *Streaming velocity field*: Streaming is a stationary flow which always has rotational character and its velocity increases with the sound intensity. However, even at the high intensity levels, the magnitude of the streaming velocity remains smaller than the acoustic velocity. The interaction between the acoustic waves in viscous fluids and solid boundaries is responsible for the generation of streaming patterns. Based on the analytical formula derived by Rott,[15] the axial (u_{st}) and transverse (v_{st}) components of the streaming velocity are

$$u_{st} = \frac{3}{8}\frac{u_{max}^2}{c_0}\left(1 - \frac{2y^2}{(H/2)^2}\right)\sin(\pi x/\ell), \tag{4}$$

$$v_{st} = -\frac{3}{8}\frac{u_{max}^2}{c_0}\frac{2\pi y}{\lambda}\left(1 - \frac{y^2}{(H/2)^2}\right)\cos(\pi x/\ell), \tag{5}$$

where y is the transverse coordinate ($-H/2 \leq y \leq H/2$), H is the width of the channel, and $\ell = \lambda/4$. As inferred from Eqs. (4) and (5), the streaming appears as four streaming vortices per half-wavelength of the acoustic wave which are symmetric about the channel center line (see Fig. 3).[16–18] The acoustic velocity is two to three orders of magnitude higher than the streaming velocity. In fact, in the acoustic wave equation, the acoustic velocity is the first order component and the streaming velocity is the second order component.

(3) *Pumped fluid velocity field*: In the valveless SWP, there is a third significant velocity field which affects both acoustic and streaming patterns and referred to as the pumped fluid velocity field. It is due to the pressure fluctuation at the outlet and the smaller fluidic resistance in the diffuser direction than that in the nozzle direction in the diffuser-nozzle element.
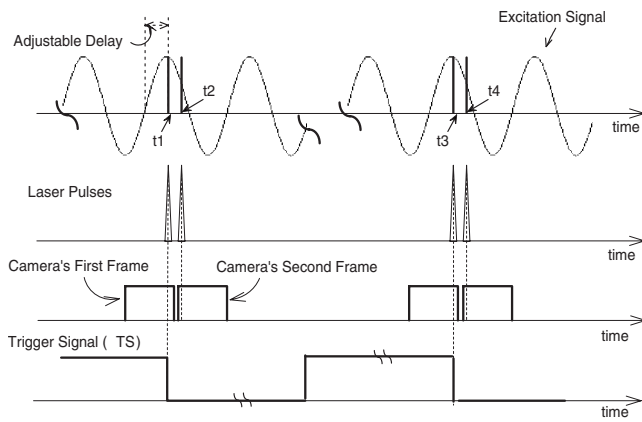
FIG. 4. The triggering sequence that shows the simultaneous measurement of the acoustic and streaming velocity fields at a particular phase of the excitation signal. t_1 and t_2 correspond to the times at which the first and second images of an image pair are captured. t_3 and t_4 are the times associated with the first and second images of the consecutive image pair.

Among these velocity fields associated with the valveless SWP, the acoustic and streaming velocity fields inside a standing wave resonator (without inlet and outlet) have been extensively studied analytically,[19] numerically,[17] and experimentally.[16,18,20,21] However, the interactions of the pumped fluid velocity field and acoustic and streaming patterns have not been investigated. The knowledge of these interactions is vital for the development of an efficient valveless SWP.

IV. SYNCHRONIZED PIV TECHNIQUE

In the particle image velocimetry (PIV) technique, positions of the flow-tracing particles are recorded at two known times by illuminating the particles using a laser light sheet. A charge coupled device (CCD) camera captures the images of the particles at each pulse in the flow field of interest. The displacement of particles between the two images divided by the time separation between the laser pulses provides the velocity field. In the conventional PIV setup, the laser pulses are synchronized with the camera frames. Typically these signals are not synchronized with any flow characteristics because for steady flows it is not necessary. However, for velocity measurements in the presence of an acoustic standing wave, two laser pulses and the camera triggering need to be synchronized with the excitation signal to capture the velocity fields at the desired phase of the standing wave. The authors have developed a novel approach using synchronized PIV to measure two-dimensional streaming velocity fields in the presence of acoustic standing wave of different frequencies and intensities.[16] The basic principle of this scheme is shown in Fig. 4. Consider the image taken at time t_1 in Fig. 4 as the first image and the image taken at time t_2 as the second image with the time separation of t_2-t_1. The cross correlation of this image pair provides the acoustic velocity field at time $(t_1+t_2)/2$. Now, consider the image taken at time t_1 as the first image and the image taken at time t_3 as the second image, with the time separation of t_3-t_1. Since the images acquired at t_1 and t_3 are exactly at the same phase,
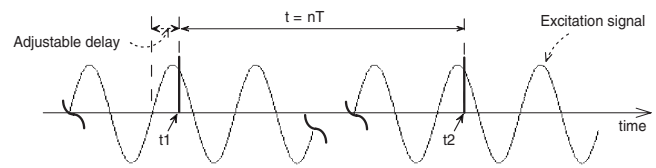

FIG. 5. The triggering sequence that shows the measurement of the streaming velocity field at a particular phase of the excitation signal. t_1 and t_2 correspond to the times at which the first and second images of an image pair are captured.

the acoustic velocity components at these times will be the same; therefore, the particle shift between these two images will only be due to streaming velocity. Thus, the cross correlation of this image pair will provide the streaming velocity field at time $(t_1+t_3)/2$.[16]

Trigger signal (TS) in Fig. 4 is used to trigger both laser and CCD camera of the PIV system. That is, both the laser and the camera are synchronized with the excitation signal via TS. The synchronization sequence for the excitation signal, laser pulses, camera frames, and TS is also shown in Fig. 4.

In the approach shown in Fig. 4, the separation time between two images utilized for the streaming velocity measurement ($\delta t=t_3-t_1$ in Fig. 4) is fixed and equal to the inverse of the camera frame rate. However, to resolve the streaming velocity fields of high magnitudes and gradients, this value of δt might be too large. As a result, the particle shift between the first and second images of the image pair will also be large. Thus, a larger interrogation window size needs to be selected which significantly reduces the spatial resolution of the measured velocity vectors. Furthermore, in cases where the streaming velocity fields are highly rotational or the velocity gradients are very high, the shape of the streaming patterns cannot be correctly captured using a large value of δt. Therefore, in such cases, δt needs to be adjusted accordingly.

In the case of high streaming velocity amplitude or gradient, the separation time is chosen to be an integer multiplication of the wave period (T), that is, $\delta t=nT$, $n=1,2,\ldots,N$ (see Fig. 5). N should be chosen so that $1/nT \leq$ frame rate of the CCD camera. The appropriate value of N should be determined for each experiment based on the maximum amplitude and gradient of the streaming velocity. For example, at the excitation frequency of $f=1000$ Hz ($T=1$ ms) and camera frame rate of 30 frames/s, N can be varied from 1 to 33. For very high amplitudes or gradient streaming flows, a small number should be chosen for N in order to reduce δt so that the streaming patterns can be correctly captured, while for slow streaming flows, a large number should be chosen for N in order to increase the signal-to-noise ratio and reduce the errors in the velocity measurements.

V. EXPERIMENTAL SETUP AND MEASUREMENTS

A test apparatus is built to measure and analyze the flow structure inside the pump chamber of the valveless SWP, as shown in Fig. 6(a). The pump chamber is a Plexiglas channel with a square cross-sectional area with the length of 74 cm and the inner cross section of 7×7 cm^2. The inner diameter
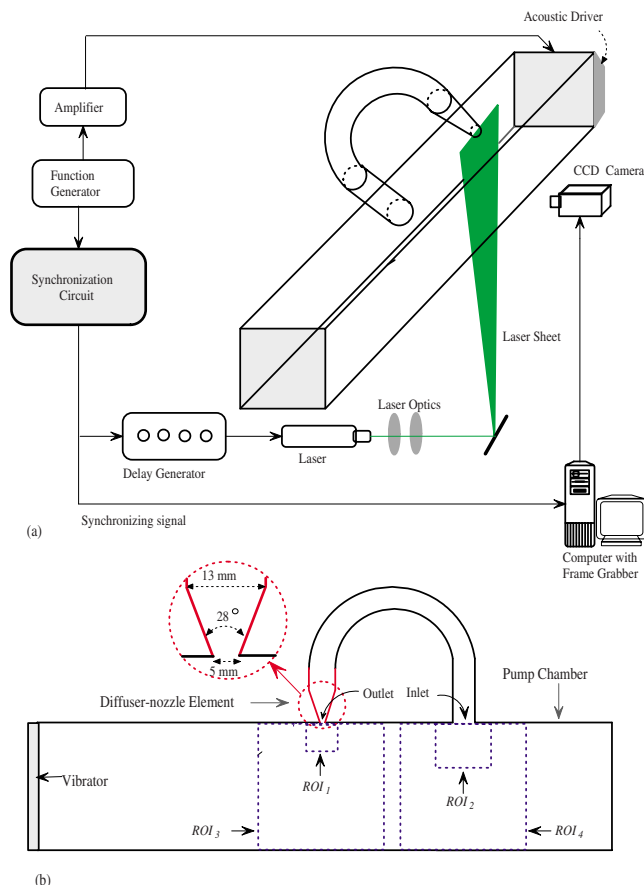
FIG. 6. (Color online) (a) Experimental setup to measure the flow structure inside the pump chamber of the valveless SWP. (b) Four ROIs in which the PIV measurements have been conducted.

of the diffuser-nozzle element at the narrowest section is 5 mm and that at the widest section is 13 mm. The half-angle of the diffuser-nozzle element (θ) is 14°. The inner diameter of the inlet is 13 mm. The inlet and outlet of the pump are connected together via a flexible plastic tube with 13 mm inner diameter in order to generate a circulatory flow inside the pump. This configuration makes it possible to keep the seed particles inside the pump for PIV measurements. The two-dimensional velocity fields inside the channel are measured using the synchronized PIV technique. The measurements are conducted in a plane parallel to the channel length at the midchannel location as shown in Fig. 6(a). The PIV measurements have been performed in four regions of interest (ROIs). The dimensions of these regions are 1.1×0.7, 3.3×2.5, 10×7.5, and 10×7.5 cm^2. Hereinafter, they are referred to as ROI$_1$ to ROI$_4$, respectively [see Fig. 6(b)].

A 120 mJ neodymium doped yttrium aluminum garnet laser (Solo PIV 120XT, New Wave Research) is used as a light source for the PIV measurements. A CCD camera (JAI, CV-M2) with the resolution of 1600×1200 pixels is used to image the flow. The camera is connected to a personal computer equipped with a frame grabber (DVR Express, IO Industries, London, ON, Canada) that acquired 8 bit images at a rate of 30 Hz. A four-channel digital delay generator (555-4C, Berkeley Nucleonics Corporation, San Rafael, CA) is used to control the timing of the laser pulses. Bis(2-

ethylhexyl) sebacate mist with the mean diameter of 0.5 μm is used as the tracer particles. The acoustic standing wave inside the tube is excited using a special loudspeaker driver. The driver had a maximum power of 200 W. The use of a loudspeaker driver as an acoustic source made it easy to vary the frequency and intensity of excitation continuously and precisely. A function generator (model Agilent 33120A) is used to generate the sinusoidal waves of different frequencies and amplitudes. The signal from the function generator is amplified by a 220 W amplifier (Pioneer SA-1270). The loudspeaker is driven by this amplified signal [see Fig. 6(a)].

A quarter-inch condenser microphone cartridge model 377A10 printed circuit board (Piezotronics) is used to measure the sound intensity level and the dynamic pressure amplitude inside the resonator when the loudspeaker is excited. The microphone is attached to a thin plastic rod and slid into the channel through a hole in the end wall in order to measure the pressure at the outlet position and is then removed for PIV measurements. The driver frequency (f) is set equal to 456 Hz. The corresponding wavelength (λ) of the acoustic standing wave is 74 cm. It allows the formation of one full standing wave inside the channel.

In order to accurately measure the periodic particle velocity, the separation time between two images must be adjusted appropriately. Due to the oscillation of the particles, the time separation between the two images of an image pair should be much less than the quarter of the wave period. Otherwise, the particle displacement computed by cross correlating the PIV images will be smaller than the actual displacement of the particles. This will result in the underestimated acoustic velocities. On the other hand, for a very short separation time, the particle shift between the two images of an image pair will be too small and will increase uncertainty in the velocity measurements. In the present cases, the time separation is set equal to 60 μs, which is nine times smaller than the quarter-wave period and still large enough to resolve the small displacements. The size of the interrogation region is set equal to 24×24 pixels and the size of the search region is set equal to 48×48 pixels. A three-point Gaussian subpixel fit scheme is used to obtain the correlation peak with subpixel accuracy. A 50% window overlap is used in order to increase the nominal resolution of the velocity field to 12×12 pixels. A scheme is used to identify the spurious velocity vectors and then correct them using a local median test.[22] The percentage of the spurious velocity vectors is less than 0.5%.

VI. RESULTS AND DISCUSSION

In this study, air at room temperature ($\rho_0 = 1.2$ kg/m^3, $\mu = 1.82 \times 10^{-5}$ kg/ms, and $c_0 = 344$ m/s) has been used as the pumped fluid. We have considered two different maximum vibrational displacements which are called hereinafter cases A and B. The values of the maximum antinode pressure amplitude (P_m) are 295 and 535 Pa for cases A and B, respectively.
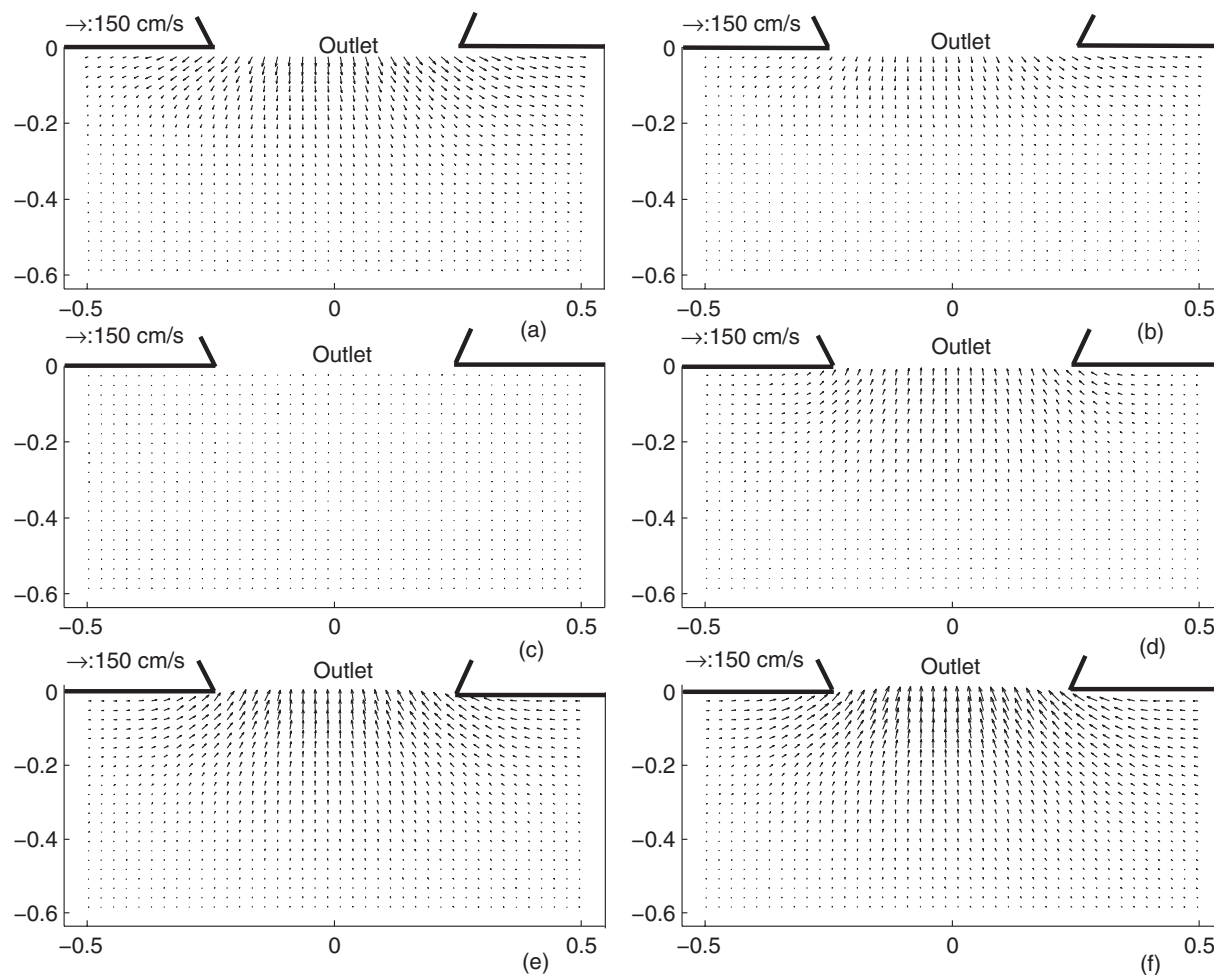
FIG. 7. Two-dimensional velocity fields for case A at six different phases: (a) $\phi=100°$, (b) $\phi=133°$, (c) $\phi=167°$, (d) $\phi=200°$, (e) $\phi=233°$, and (f) $\phi=267°$. Horizontal axis is the axial location in cm; vertical axis is the transverse location in cm. The velocity fields are measured in the ROI_1 region. (0,0) coordinate corresponds to the middle of outlet orifice (enhanced online).

A. Net flow rate of the pump

By adjusting the time delay in the synchronization circuit, the measurements have been performed at 21 phases of the pressure signal in the ROI_1 region [see Fig. 6(b)]. For each phase of the excitation voltage, 100 PIV images are captured. From these images, 50 acoustic velocity fields are computed which are averaged in order to enhance the signal-to-noise ratio. The averaged velocity fields at six different phases of the pressure signal [see Fig. 2(a)], which are $\phi=100°$, 133°, 167°, 200°, 233°, and 267° for cases A and B, are shown in Figs. 7 and 8, respectively.

The mean velocities at the outlet at different phases (ϕ) for cases A and B are plotted in Fig. 9. This parameter is computed by integrating the velocity amplitudes over the outlet sectional area.

The plots in Figs. 7 and 8 show the transitional behavior of the velocity fields inside the pump chamber and near the outlet over the half-period of the excitation signal. Figures 7(a), 7(b), 8(a), and 8(b) depict the transient flow rate at $\phi=100°$ and 133°, where the pressure at the outlet (pressure antinode) is below P_0. Therefore, the fluid is sucked into the pump chamber. At $\phi=167°$ the pressure at the outlet is almost equal to P_0, which results in almost zero velocity [see

Figs. 7(c) and 8(c)], whereas, at $\phi=200°$, 233°, and 267° [Figs. 7(d)–7(f) and 8(d)–8(f)], the pressure at the outlet is larger than P_0, which makes the fluid pump out of the pump chamber. However, as shown in Fig. 9, due to less flow resistance in the diffuser than that in the nozzle direction, the mean velocities in the diffuser direction (positive cycles) are larger than those of the nozzle direction (negative cycles). This causes a net flow discharge through the outlet. It must be noted that the velocity field inside the pump chamber is the superposition of the three velocity fields, the pumping fluid, acoustic, and streaming fields. However, since the outlet is located at the velocity node (pressure antinode), the amplitude of the acoustic velocity at the outlet is almost zero. The amplitude of the streaming velocity is also negligible compared to the pumped fluid velocity. Therefore, the velocity fields depicted in Figs. 7 and 8 are almost entirely due to the pumped fluid velocity field.

In order to quantify the performance of the valveless SWP, the values of the maximum, minimum, and overall net velocities at the outlet (U_{max}, U_{min}, and U_{net}, respectively), the net flow rate ($Q=U_{net} \times A_{outlet}$), the maximum Reynolds number ($Re_{max}=\rho U_{max} D_{outlet}/\mu$), pressure loss coefficients, and rectification capability [Eqs. (2) and (1)] for both cases A
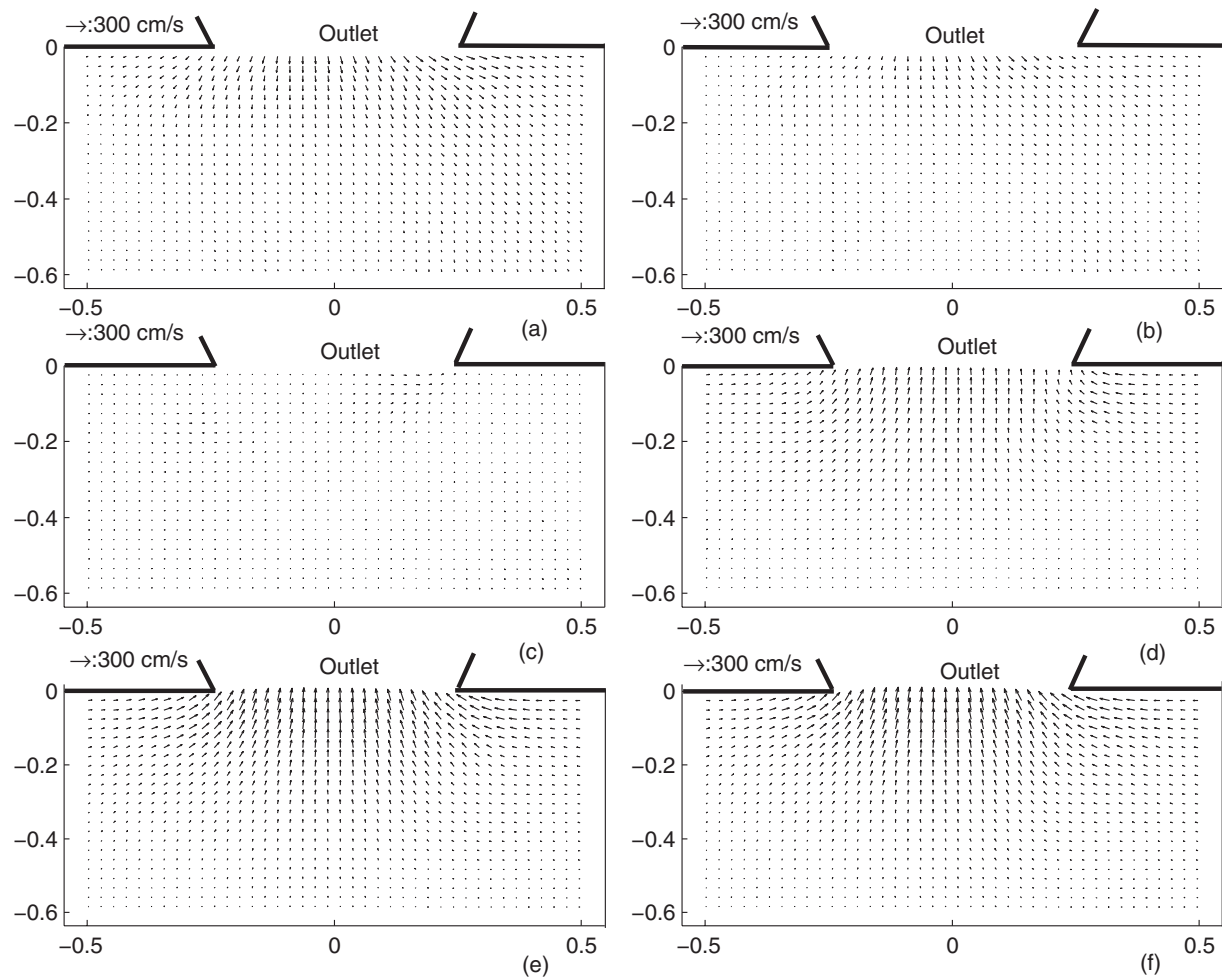
FIG. 8. Two-dimensional velocity fields for case B at six different phases: (a) $\phi=100°$, (b) $\phi=133°$, (c) $\phi=167°$, (d) $\phi=200°$, (e) $\phi=233°$, and (f) $\phi=267°$. Horizontal axis is the axial location in cm, Vertical axis is the transverse location in cm. The velocity fields are measured in the ROI$_1$ region. (0,0) coordinate corresponds to the middle of outlet orifice.

and B are presented in Table I. A_{outlet} and D_{outlet} are the area and diameter of the outlet orifice, respectively. The results in Table I show that the values of ξ_d are always smaller than those of ξ_n, which is related to lower flow impedance in the

diffuser direction than that in the nozzle direction. Table I also shows that for the cases studied, the rectification capability and the net flow rate increase with an increase in the maximum pressure (or Reynolds number). This observation is in agreement with the previous numerical and experimental analyses of the reciprocating valveless pumps.[8,23–25]
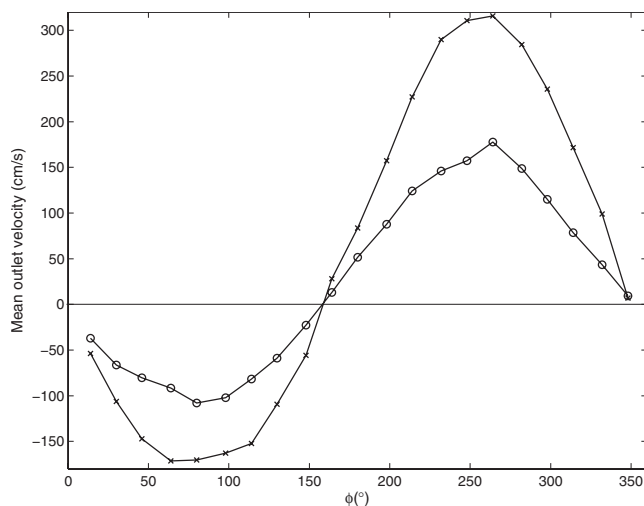

FIG. 9. The mean velocity at the outlet vs phase for case A (○) and case B (×).

TABLE I. Maximum antinode pressure (P_m), maximum, minimum, and overall net velocities at the outlet (U_{max}, U_{min}, and U_{net}, respectively), maximum Reynolds number (Re$_{max}$), pressure loss coefficients (ξ_n and ξ_d), rectification capability (η), and net flow rate (Q) of the tested valveless SWP for cases A and B.

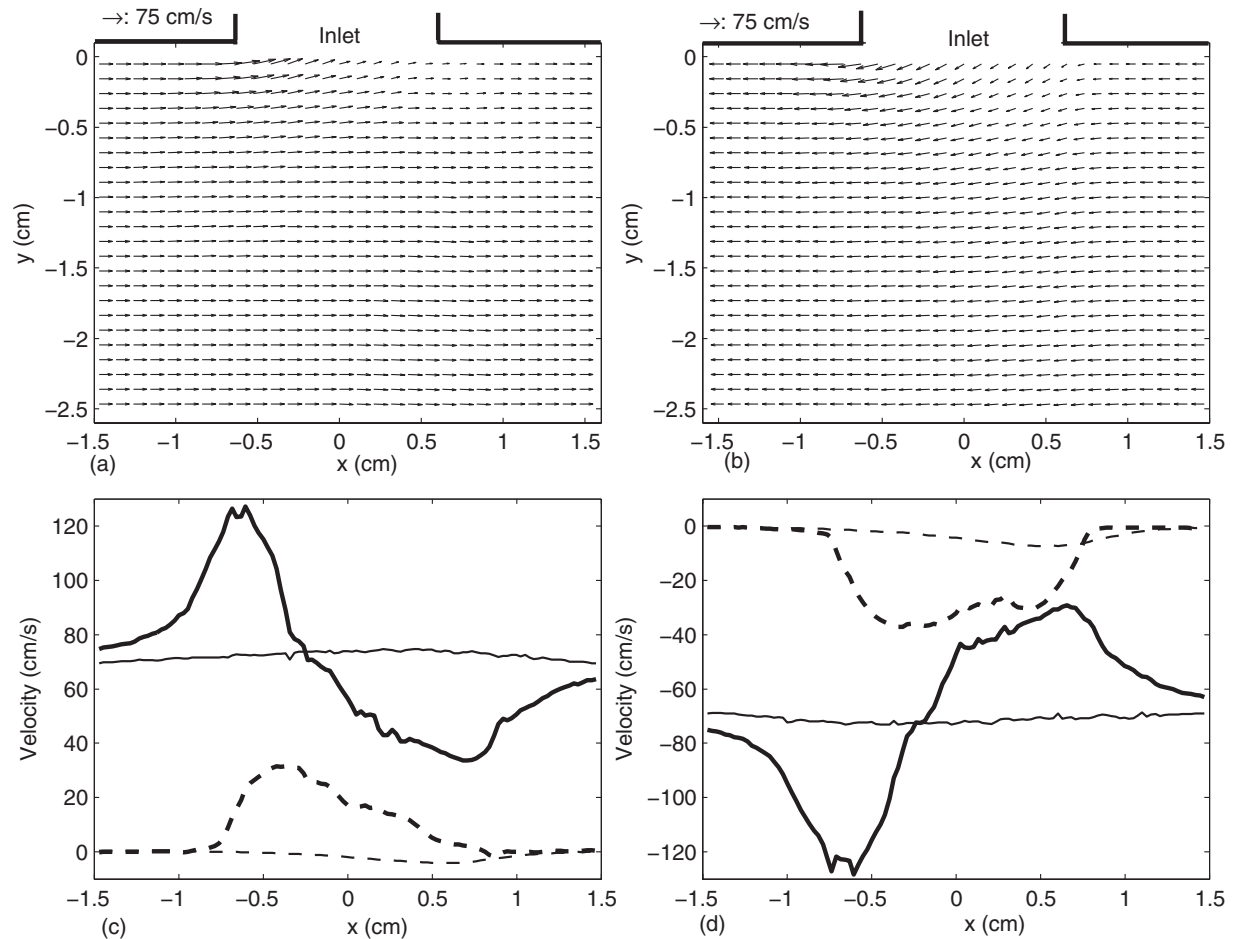|	Case A	Case B
P_m (Pa)	295	535
U_{max} (cm/s)	177.8	315.8
U_{min} (cm/s)	−107.8	−171.5
U_{net} (cm/s)	24.0	51.5
Re$_{max}$	588	1045
ξ_n	422	302
ξ_d	155	89
η	2.72	3.39
Q (ml/min)	283	606

FIG. 10. The phased-averaged velocity fields at the inlet for case A at (a) $\phi=100°$ and (b) $\phi=267°$. The axial (solid line) and transverse (dashed line) components of the total velocity field at $y=-0.05$ cm (thick) and $y=-2.5$ cm (thin) at (c) $\phi=100°$ and (d) $\phi=267°$. The velocity fields are measured in the $\mathrm{ROI_2}$ region. (0,0) coordinate corresponds to the middle of the inlet orifice.

B. Interaction of different velocity fields inside the pump chamber

In Sec. VI A, the pumping action of the valveless SWP without using any moving component or check valve has been demonstrated at two different pressure amplitudes. In this section, we have analyzed the interactions of different velocity fields inside the chamber of this novel pump.

The structure of the velocity field due to the pumped fluid velocity in the vicinity of the outlet has already been shown in Figs. 7 and 8. The interaction of the pumped fluid and acoustic field cannot be investigated in the outlet region as the acoustic velocity is almost zero at the outlet (because the outlet is located at the velocity node or pressure antinode). Thus, the effect of the pumped fluid velocity field on the acoustic velocity is investigated in the vicinity of the inlet ($\mathrm{ROI_2}$ region), which is located at the velocity antinode, where the acoustic velocity amplitude is maximum. The velocity fields at two different phases ($\phi=100°$ and 267°), which almost correspond to the extremum of the acoustic velocity, are shown in Fig. 10.

Figures 10(a) and 10(b) show that the acoustic velocity vectors are disturbed by the pumped flow field in the region close to the inlet. This effect has been illustrated in Figs. 10(c) and 10(d) as well, where the variations in the axial

and transverse components of the total velocity fields with respect to x at $y=-0.05$ cm (close to the inlet) and $y=-2.5$ cm are depicted. As shown in these figures, both axial and transverse components of the acoustic velocity drastically deviate from the ones without inlet and outlet at $y=-0.05$ cm (close to the inlet). This influence reduces with the distance away from the inlet location in both the x and y directions. At $y=-2.5$ cm, the shape and amplitude of the axial acoustic velocity are close to the theoretical one in a closed chamber. The theoretical value of the maximum axial acoustic velocity (u_{max}) in a closed chamber, i.e., without inlet and outlet, for $P_m=295$ Pa is 71 cm/s. Figure 10 also shows that the effect of the pumped flow field on the acoustic velocity is negligible outside the 3×3 cm² region from the center of the inlet. Figures 10(c) and 10(d) show that the waveforms of the axial component of the total velocity close to the inlet at $\phi=100°$ and $\phi=267°$ are almost reversed.

In order to investigate the effect of the pumped flow field on the streaming velocity, it is necessary to remove the effect of the acoustic velocity. This can be done using the technique described in Sec. IV. By choosing $n=1$ in Fig. 5, the separation time between two PIV images would be equal to $T=1/f=2193$ μs. The velocity fields that are composed of the streaming and the pumped flow velocities (the acoustic ve-
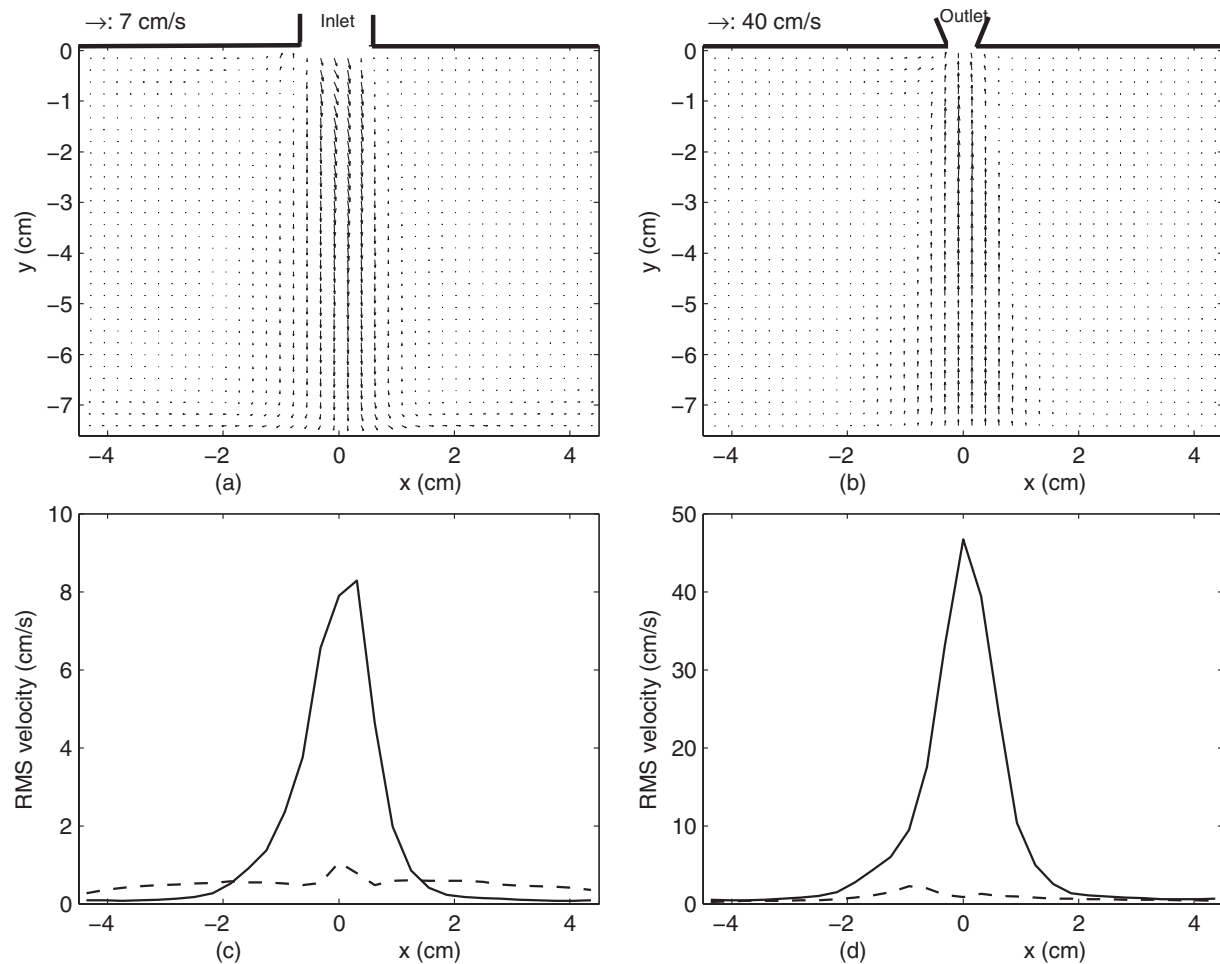
FIG. 11. The total pumped and streaming velocity vectors (a) at the inlet measured in the ROI_4 region (left pane) and (b) at the outlet measured in the ROI_3 region (right pane) for case A. The rms axial (dashed line) and rms transverse (solid line) components of the total velocity field (c) at the inlet and (d) at the outlet. (0,0) coordinate corresponds to the middle of the inlet orifice for the left panel and the middle of the outlet orifice for the right panel.

locity has been removed) at the inlet (measured in the ROI_4 region) and outlet (measured in the ROI_3 region) of the valveless SWP are shown in Figs. 11(a) and 11(b). In order to compute the rms streaming velocity, the velocity data in the ROI were extracted at each axial location over the height of the ROI. The rms velocity at each axial location was computed from these data. The rms of the axial and transverse components of the velocity in the ROI_4 and ROI_3 regions are shown in Figs. 11(c) and 10(d). The theoretical values of the maximum axial ($u_{st\ max}$) and transverse ($v_{st\ max}$) components of streaming velocity in a closed chamber for $P_m = 295$ Pa are 0.057 and 0.016 cm/s, respectively. As seen, the amplitude of the streaming is 1200 times smaller than the axial acoustic velocity ($u_{max} = 71$ cm/s). The overall shape of the streaming patterns in a closed chamber, i.e., without inlet and outlet, is similar to that shown in Fig. 3 with the maximum velocity of 0.057 cm/s (for $P_m = 295$ Pa). However, with inlet and outlet, these symmetric and low velocity patterns are deformed to the patterns shown in Fig. 11 with maximum velocity of almost 40 cm/s. That is, the streaming patterns drastically deviate from the ones without inlet and outlet due to the pumped flow field. Furthermore, the maximum rms velocity at the outlet is almost six times larger than that at the

inlet, which is due to the fact that the area of the outlet orifice is almost six times smaller than that of the inlet.

Another important observation in Figs. 11(a) and 11(b) is described as follows. The velocity fields shown in Figs. 11(a) and 11(b) are captured at the same phase of consecutive cycles of the excitation signal. Therefore, the effect of the acoustic velocity field is removed. The streaming velocity field is also negligible compared to the pumped flow field. Thus, the resultant velocity vectors shown in Figs. 11(a) and 11(b) are the overall pumped flow at the inlet and outlet of the valveless SWP over a period of the excitation signal. As shown in Fig. 11(a), at the inlet an overall flow suction into the pump chamber is observed. However, at the outlet [Fig. 11(b)], an overall flow discharge out of the pump chamber is observed.

VII. CONCLUSION

The operating principle of the valveless SWP is described. The two-dimensional unsteady velocity fields inside the chamber of this novel pump at different phases of the excitation signal are measured using the synchronized PIV technique. The variations in the pump flow rate, pressure loss

coefficients, and rectification capability of the diffuser-nozzle element are analyzed. The results show that this pump is capable of pumping fluid and for the cases studied; its net flow rate increases with an increase in the maximum pressure (or Reynolds number). Furthermore, the interactions of three different flow fields inside the pump chamber are studied. It is found that while the pumping flow has a slight effect on the acoustic velocity patterns (mainly around the inlet and outlet), the streaming velocity structures are drastically affected by the pumping flow.

ACKNOWLEDGMENTS

[1] B. L. Smith and A. Glezer, "The formation and evolution of synthetic jets," Phys. Fluids **10**, 2281 (1998).

[2] E. Jung and C. S. Peskin, "Two-dimensional simulations of valveless pumping using the immersed boundary method," SIAM J. Sci. Comput. (USA) **23**, 19 (2001).

[3] A. I. Hickerson, D. Rinderknecht, and M. Gharib, "Experimental study of the behavior of a valveless impedance pump," Exp. Fluids **38**, 534 (2005).

[4] G. Manopoulos, D. S. Mathioulakis, and S. G. Tsangaris, "One dimensional model of valveless pumping in a closed loop and a numerical solution," Phys. Fluids **18**, 017106 (2006).

[5] A. I. Hickerson, D. Rinderknecht, and M. Gharib, "A valveless micro impedance pump driven by electromagnetic actuation," J. Micromech. Microeng. **15**, 861 (2006).

[6] T. T. Bringley, S. Childress, N. Vandenberghe, and J. Zhang, "An experimental investigation and a simple model of a valveless pump," Phys. Fluids **20**, 033602 (2008).

[7] E. Stemme and G. Stemme, "A valveless diffuser/nozzle-based fluid pump," Sens. Actuators, A **39**, 159 (1993).

[8] A. Olsson, G. Stemme, and E. Stemme, "A numerical design study of the valveless diffuser pump using lumped-mass mode," J. Micromech. Microeng. **9**, 34 (1999).

[9] H. Mandorian, "Standing wave pump," U.S. Patent No. 3743446 (3 July 1973).

[10] T. Lucas, "Standing wave compressor," U.S. Patent No. 5020977 (4 June 1991).

[11] R. Bishop, "Standing wave pump," U.S. Patent No. 6079214 (27 June 2000).

[12] M. Kawahashi, F. Tamotsu, and M. Saito, "Acoustic fluid machine," U.S. Patent No. 7252178B2 (7 August 2007).

[13] T. Gerlach and H. Wurmus, "Working principle and performance of the dynamic micropump," Sens. Actuators, A **50**, 135 (1995).

[14] Y. C. Wang, J. C. Hsu, P. C. Kuo, and Y. C. Lee, "Loss characteristics and flow rectification property of diffuser valves for micropump applications," Int. J. Heat Mass Transfer **52**, 328 (2009).

[15] N. Rott, "The influence of heat conduction on acoustic streaming," Z. Angew. Math. Phys. **25**, 417 (1974).

[16] M. Nabavi, K. Siddiqui, and J. Dargahi, "Simultaneous measurement of acoustic and streaming velocities using synchronized PIV technique," Meas. Sci. Technol. **18**, 1811 (2007).

[17] A. Alexeev and C. Gutfingera, "Resonance gas oscillations in closed tubes: Numerical study and experiments," Phys. Fluids **15**, 3397 (2003).

[18] M. Nabavi, K. Siddiqui, and J. Dargahi, "Experimental investigation of the formation of acoustic streaming in a rectangular enclosure using a synchronized PIV technique," Meas. Sci. Technol. **19**, 065405 (2008).

[19] Y. A. Ilinskii, B. Lipkens, T. S. Lucas, and T. W. Van Doren, "Nonlinear standing waves in an acoustical resonator," J. Acoust. Soc. Am. **104**, 2664 (1998).

[20] M. Nabavi, K. Siddiqui, and J. Dargahi, "Measurement of the acoustic velocity field of nonlinear standing wave using the synchronized PIV technique," Exp. Therm. Fluid Sci. **33**, 123 (2008).

[21] M. Nabavi, K. Siddiqui, and J. Dargahi, "Effects of transverse temperature gradient on acoustic and streaming velocity fields in a resonant cavity," Appl. Phys. Lett. **93**, 051902 (2008).

[22] K. Siddiqui, M. R. Loewen, C. Richardson, W. E. Asher, and A. T. Jessup, "Simultaneous particle image velocimetry and infrared imagery of microscale breaking waves," Phys. Fluids **13**, 1891 (2001).

[23] K. S. Yang, I. Y. Chen, B. Y. Shew, and C. C. Wang, "Investigation of the flow characteristics within a micronozzle/diffuser," J. Micromech. Microeng. **14**, 26 (2004).

[24] C. L. Sun and K. H. Huang, "Numerical characterization of the flow rectification of dynamic microdiffusers," J. Micromech. Microeng. **16**, 1331 (2006).

[25] H. J. Sheen, C. J. Hsu, T. H. Wu, C. C. Chang, H. C. Chu, C. Y. Yang, and U. Lei, "Unsteady flow behaviors in an obstacle-type valveless micropump by micro-PIV," Microfluid. Nanofluid. **4**, 331 (2008).